CrystEngComm

ROYAL SOCIETY OF CHEMISTRY

PAPER

View Article Online
View Journal

Cite this: DOI: 10.1039/d5ce01141h

Metal-ion-dependent polarity switching and dielectric enhancement in solvent-vapour-responsive mononuclear complexes

Fumiya Kobayashi, *[a] Hiroki Iwase,[a] Shoma Hoshino [b] and Makoto Tadokoro *[a]

Received 2nd December 2025,
Accepted 6th May 2026

DOI: 10.1039/d5ce01141h

rsc.li/crystengcomm

Design of molecular materials that exhibit multiple cooperative responses to external stimuli is a key challenge in the development of next-generation functional materials. Herein, we report solvent-vapour-responsive mononuclear Fe(III) and Mn(III) complexes, [M(azdp)(acac)(sol)] (M = Fe, Mn; H_2azdp = 2,2′-azodiphenol; sol = MeOH, DMSO), which undergo solvent-vapour-driven structural transformations between polar and nonpolar molecular assemblies through ligand exchange at the solvent coordination site. The Fe(III) complexes exhibited pronounced cooperative aggregation upon DMSO coordination, generating polar molecular packings that showed strong second harmonic generation (SHG), enhanced dielectric constants, and ferroelectric-like relaxor behaviour. By contrast, the Mn(III) analogues form centrosymmetric dimers stabilised by Jahn–Teller distortion, resulting in nonpolar assemblies and SHG inactivity. These findings revealed a direct relationship between the metal-centred electronic structure, ligand geometry, and aggregation-induced functionality. The cooperative transformations integrate optical and dielectric functionalities within a single molecular platform, demonstrating a generalisable strategy for constructing solvent-vapour-responsive polar coordination materials.

Introduction

Molecular assemblies in the solid state play a key role in governing collective properties such as magnetism, ferroelectricity, electrical conductivity, and nonlinear optical (NLO) responses of molecular solids.[1–13] The development of molecular solid materials in which subtle structural changes can be precisely controlled by external stimuli has emerged as a promising strategy for realising next-generation functional materials.[14–21] In particular, solvent-responsive systems that show reversible transformations such as vapochromism and magnetic switching have attracted significant interest.[22–38] However, the coupling of dielectric and optical functionalities within a single-coordination framework remains largely unexplored and currently is poorly understood.

Recent studies have demonstrated that guest molecules can be used to control the polar alignment of molecular structures and dielectric properties in crystalline solids,[39–44] and these systems have been systematically classified by Ohtani and co-workers.[45] In this context, we previously reported solvent-induced reversible switching between polar and nonpolar assemblies in mononuclear complexes [M(sap)(acac)(sol)] (M = Fe, Al; H_2sap = 2-salicylideneaminophenol, acac = acetylacetonate).[46–48] These findings suggest that subtle differences in the solvent coordination environments can trigger cooperative structural transformations, providing valuable design principles for the intentional control of molecular packing polarity. Nevertheless, fundamental questions remain regarding the correlation between the characteristics related to the metal centres such as spin states and Jahn–Teller distortion and the solvent-induced structural reorganisation, as well as the possible extension of the range of ligand systems toward versatile and generalisable frameworks. Understanding how metal-ion electronic configurations control the macroscopic polar ordering is essential for rational design of multifunctional materials.

In this study, we sought to elucidate the relationships between characteristics of the metal centres and the macroscopic properties by extending both the range of studied ligand architectures and the types of central metal ions. The tridentate ligand 2,2′-azodiphenol (H_2azdp), which is structurally analogous to H_2sap but incorporates an azo group instead of the imine moiety, was selected to investigate how the absence of the imine proton affects the intermolecular interactions governing aggregation structures (Scheme 1). In addition, the replacement of Fe(III) with

[a] Department of Chemistry, Faculty of Science, Tokyo University of Science, 1-3, Kagurazaka, Shinjuku-ku, Tokyo 162-8601, Japan. E-mail: fkobayashi@rs.tus.ac.jp
[b] Department of Chemistry, School of Science, Kitasato University, 1-15-1, Kitazato, Minami-ku, Sagamihara-shi, Kanagawa 252-0373, Japan

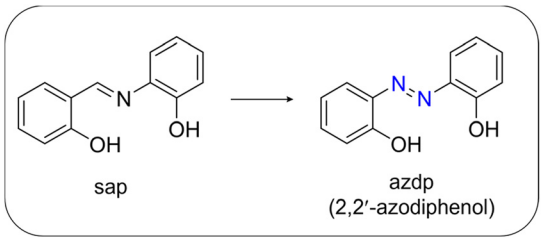

Scheme 1 Molecular structure of sap and azdp.

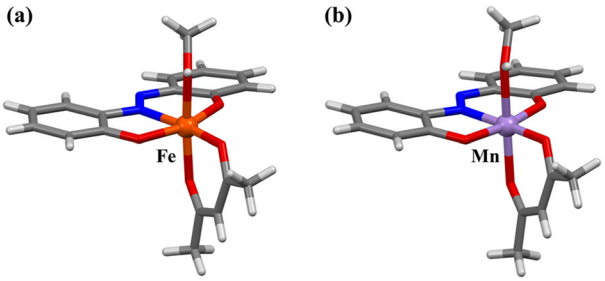

Fig. 1 Crystal structures of (a) **1** at 173 K and (b) **2** at 90 K.

Mn(III), a metal ion that typically exhibits pronounced Jahn–Teller distortion, is expected to provide insight into the metal-dependent cooperative structural behaviour.

Herein, we report the synthesis, crystal structure, and multifunctional properties of mononuclear [M(azdp)(acac)(sol)] complexes (M = Fe, Mn; sol = MeOH, DMSO). By comparing the solvent-dependent aggregation structures of the Fe(III) and Mn(III) analogues, we directly link metal ion characteristics, intermolecular interactions, packing symmetry, and polarity switching. This molecular design strategy enables cooperative transformations that affect both dielectric and second-harmonic-generation (SHG) responses, thereby providing fundamental insights into construction of multifunctional polar molecular assemblies.

Results and discussion

Syntheses and single-crystal structural analyses

Mononuclear complexes [Fe(azdp)(acac)(MeOH)] (**1**) and [Mn(azdp)(acac)(MeOH)] (**2**) were synthesised by refluxing equimolar H_2azdp with M(acac)$_3$ (M = Fe, Mn) in methanol. Single crystals suitable for X-ray diffraction (XRD) analysis were obtained by recrystallization from methanol, whereas the DMSO analogues (**3** and **4**) were prepared by the recrystallisation of **1** and **2** from mixed DMSO/methanol solutions. Additionally, DMSO-coordinated samples **1′** and **2′** were prepared by exposing **1** and **2**, respectively, to DMSO vapour. Solvent exchange was confirmed using powder X-ray diffraction (PXRD), thermogravimetric analysis (TGA), and elemental analysis. All compounds were further characterised by single-crystal XRD, PXRD, Fourier-transform infrared (FT-IR) spectroscopy, and elemental analysis (Fig. S1 and S2, SI).

Single-crystal X-ray structures of **1** and **2** were obtained at 173 and 90 K, respectively, and the obtained crystallographic data are presented in Table S1 (SI). **1** crystallised in the $P2_1/c$ monoclinic space group (Fig. 1a and S3, SI). The structure of **1** was similar to the previously reported structures of metal complexes incorporating the sap ligand [M(sap)(acac)(MeOH)] (M = Fe, Al).[46,47] The Fe(III) centre has an NO_5-donor coordination sphere with a distorted octahedral geometry. The metal centre has an equatorially coordinated NO_3-donor set arising from the azdp and acac ligands, whereas the axial positions are occupied by the O and O′ donors from acac and MeOH, respectively. Each [Fe(azdp)(acac)(MeOH)] molecule is chiral and exists as a pair of enantiomers, in which the coordination planes of the ligands are oriented in opposite directions. The molecules form dimers with the opposite enantiomer by complementary hydrogen-bonding between coordinated MeOH molecules and phenol oxygen atoms from the azdp ligands (O(2)–O(5) = 2.592(2) Å) (Fig. 2). Each dimer interacts with its neighbouring dimers *via* π–π interactions. **2** has an identical structure to that of **1** and also forms dimers through hydrogen bonding (O(1)–O(5) = 2.671(6) Å) (Fig. 1b and S4 and S5, SI). Therefore, crystals of **2** in the $P2_1/c$ monoclinic space group formed a nonpolar aggregated structure. Subsequently, single-crystal XRD analyses of the DMSO-coordinated Fe–DMSO and Mn–DMSO crystals were performed at 90 K. Complex **3** forms an octahedral six-coordinate structure similar to that of **1**, in which a DMSO molecule replaces the coordinated MeOH; however, a significant distortion of the phenol ring was observed (Fig. 3a and S6, SI). The Fe–O bond lengths were obtained as Fe–O1 = 1.91(2) Å, Fe–O2 = 2.00(2) Å, Fe–O3 = 1.986(3) Å, Fe–O4 = 2.018(2) Å, and Fe–O5 = 2.043(3) Å, showing characteristic bond lengths of a high-spin Fe^{3+} ion. Complex **3** exhibits a polar packing structure along the *c*-axis through intermolecular CH–O and CH–π interactions between the coordinated DMSO molecules and the azdp ligands (Fig. 4a and S7, SI). Accordingly, **3** crystallised in the *Cc* monoclinic space group, forming a polar assembly structure. This polar packing arrangement is quite similar to that of a previously reported [Fe(sap)(acac)(DMSO)] iron complex.[46]

By contrast, the Mn–DMSO complex **4** crystallised in the $P\bar{1}$ triclinic space group, forming a packing arrangement distinct from that of **3**. Complex **4** adopts a six-coordinate octahedral geometry similar to that of **3**, with a coordinated DMSO molecule; however, the phenol ring plane is relatively flat (Fig. 3b and S8, SI). The Mn–O bond lengths were obtained as Mn–O1 = 1.820(5) Å, Mn–O2 = 1.962(5) Å, Mn–O3 = 1.959(1) Å, Mn–O4 = 2.168(2) Å, and Mn–O5 = 2.215(1) Å, indicative of a pronounced Jahn–Teller distortion along the DMSO coordination axis—a characteristic of high-spin Mn^{3+} ions. Complex **4** formed a dimeric structure *via* complementary CH–O interactions mediated by DMSO molecules, generating an inversion centre (Fig. 4b). The dimers were further connected through π–π interactions, resulting in a nonpolar packing structure (Fig. S9, SI). The formation of this inversion centre is considered to result from the elongation of the axial axis due to the Jahn–Teller effect of the Mn^{3+} ion, which provides sufficient space for the [Mn(azdp)(acac)(DMSO)]

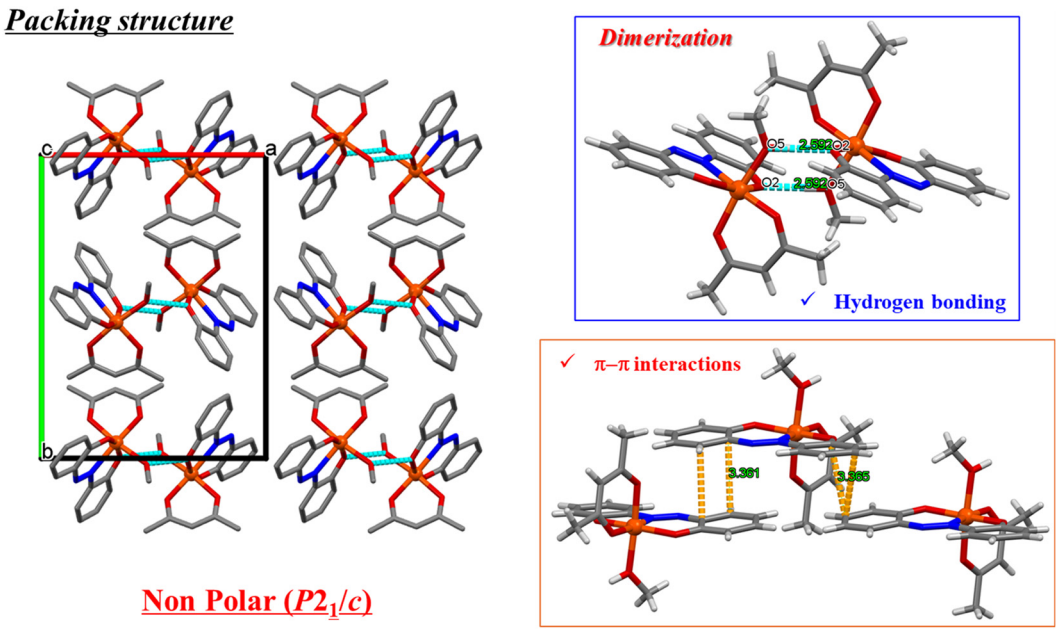

Fig. 2 Crystal packing structure and intermolecular interactions of **1** at 173 K. Blue dashed lines present hydrogen bonding.

molecules to face each other in a sterically favourable manner. Thus, Fe(III) favours polar packing because of its flexible coordination geometry, whereas Mn(III) stabilises centrosymmetric dimers owing to the pronounced Jahn–Teller distortion. The solvent coordination triggers pronounced reorganisation in the hydrogen-bond network and π–π interactions, suggesting that cooperative intermolecular forces play a key role in driving the structural transformation.

Next, the solvent-vapour responsiveness of each complex was investigated. When the methanol-containing complex **1** was exposed to DMSO vapour for 5 d, the initial PXRD patterns of **1** changed to the different patterns of **1′** (Fig. S10, SI). The observed PXRD patterns correspond to those of DMSO-coordinated **3** (Fig. S11, SI). This result was consistent with the replacement of the coordinated solvent by DMSO upon exposure to DMSO vapour, resulting in structural rearrangements of the polar (*Cc*) structure. A similar structural transformation was observed for the Mn complexes. Specifically, exposure of the MeOH-coordinated complex **2** to DMSO vapour resulted in the formation of a different powder pattern, denoted as **2′** (Fig. S11, SI). This pattern was identical to that of **4**, indicating that the coordinated solvent was replaced by DMSO upon exposure to vapour. However, the transformation of the Mn complex proceeded much more slowly compared with that of the Fe complex, requiring approximately four weeks to complete (Fig. S12, SI). This sluggish conversion reflects the substitutional inertness of the Mn^{3+} ion, again demonstrating the metal-ion dependence of the solvent-exchange behaviour. This structural transformation was further supported by PXRD, FT-IR, TGA, and elemental analyses (Fig. S13 and S14, SI). This structural transformation does not occur reversibly and spontaneously, which can be attributed to the higher coordination ability of DMSO than MeOH. Such solvent-vapour-induced transformation offers an attractive route for externally controllable optical and dielectric properties.

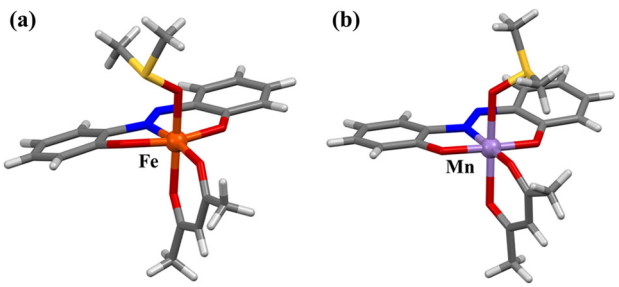

Fig. 3 Crystal structures of (a) **3** and (b) **4** at 90 K. Disordered atoms are omitted for clarity.

Dielectric properties

Compounds with polar packing structures are of particular interest, because they often exhibit unique dielectric responses and NLO effects.[49–51] To explore the impact of solvent coordination, we investigated the difference in the properties of the complexes before and after exposure to DMSO vapour. The polar nature of the structures was first assessed by SHG measurements. Emission spectra were recorded under irradiation with a 1064 nm yttrium–aluminium–garnet (YAG) laser for the MeOH-coordinated Fe(III) and Mn(III) complexes, as well as for the DMSO-exposed samples **1′** and **2′**. While no SHG response was observed for the MeOH-coordinated Fe(III) complex (Fig. 5, black line), the DMSO-exposed Fe(III) complex **1′** displayed a distinct emission band at 532 nm, corresponding to SHG (Fig. 5, blue line). This signal reflects the formation of the polar aggregated structure of **3**, which crystallises in the *Cc*

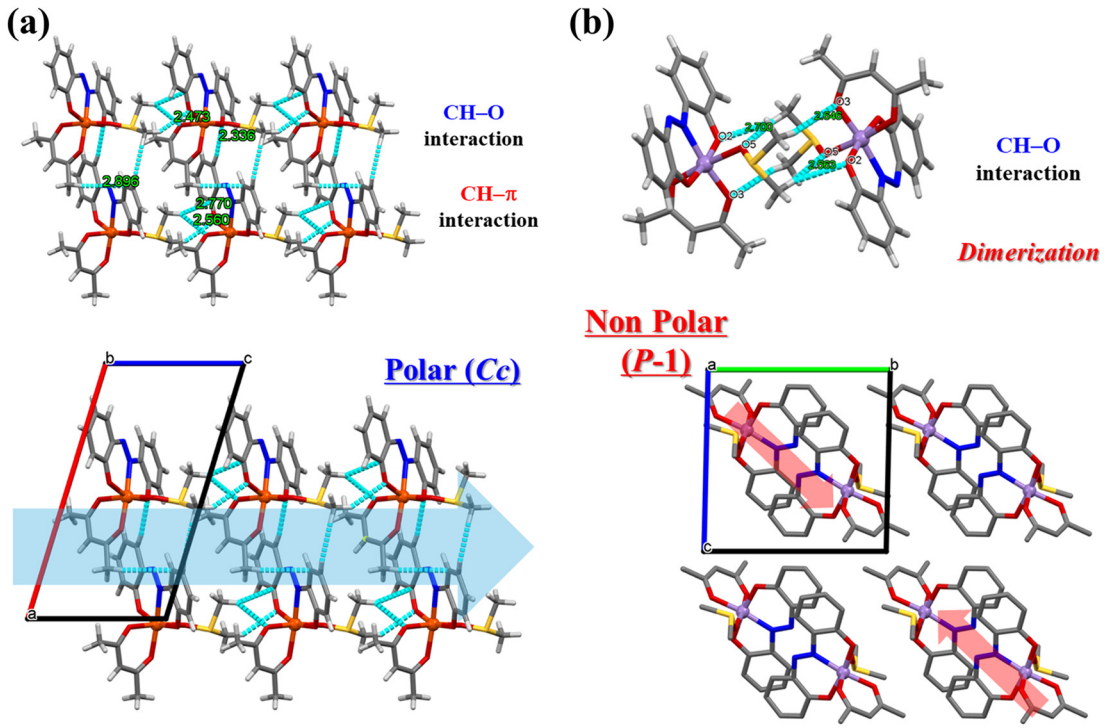

Fig. 4 Crystal packing structures and intermolecular interactions of (a) **3** and (b) **4** at 90 K. Cyan dashed lines represent CH–O and CH–π interactions. Disordered atoms are omitted for clarity.

noncentrosymmetric space group. By contrast, SHG was not detected for the DMSO-exposed Mn(III) sample **2′** (Fig. 5, red line). These results demonstrate that SHG signals serve as direct evidence of the solvent-vapour-induced transformation into polar aggregates, demonstrating that solvent coordination enables symmetry control on demand. SHG activity was absent in the nonpolar MeOH complexes but was pronounced in the DMSO derivatives (**1′**), confirming the formation of noncentrosymmetric packing.

The dielectric responses associated with the structural transformation before and after exposure to solvent vapour were measured. Variable-temperature dielectric measurements from 200 to 300 K revealed that **1** exhibited a constant value of the dielectric constant in the examined frequency range with a relative dielectric constant of 2.8 at 300 K (Fig. 6). By contrast,

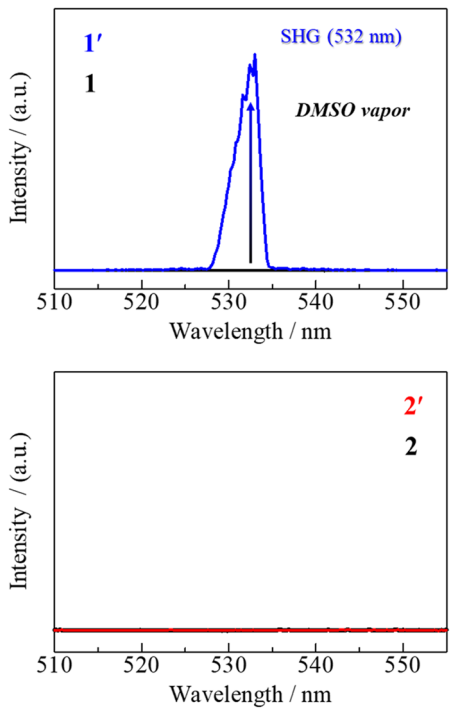

Fig. 5 SHG experiments before and after exposure to DMSO vapor for **1** (top) and **2** (bottom). YAG-laser excitation at 1064 nm.

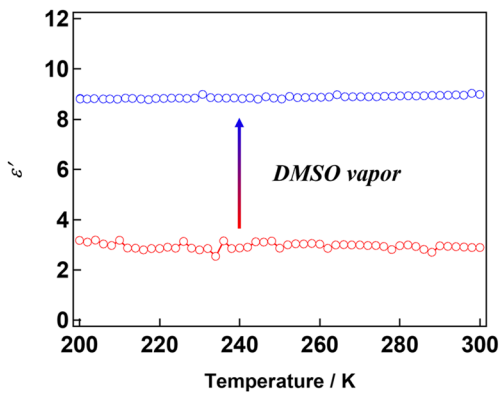

Fig. 6 Temperature-dependent ε' at AC frequencies of 10^5 Hz for pellet samples of **1** (red) and **1′** (blue) between 200 and 300 K.

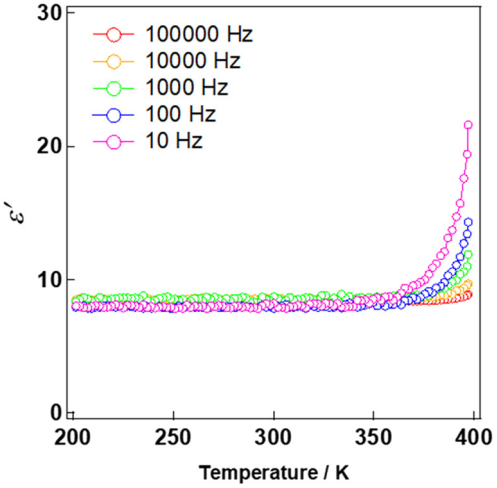

Fig. 7 Temperature-dependent ε' measured at various AC frequencies for pellet sample of **1′** between 200 and 400 K.

sample **1′**, which was obtained after exposure to DMSO vapour, showed an increased dielectric constant, reaching 8.3 at 300 K—approximately four times higher than that of **1**. The increase in the dielectric constant reflects its transformation into a polar packing structure. A similar change in the relative dielectric constant was observed in a previously reported [Al(sap)(acac)(DMSO)] aluminium complex.[47] Furthermore, the frequency dependence of the relative dielectric constant of **1′** was investigated over the temperature range of 200–400 K (Fig. 7). A pronounced frequency dependence was observed at approximately 350 K—a characteristic of relaxor-type ferroelectrics.[52–54] This behaviour likely arises from the dynamic contributions of coordinated solvent molecules and other mobile components. Solid-state NMR studies will be carried out in the future work to gain further insight into these dynamics.

Conclusions

We demonstrate that mononuclear [M(azdp)(acac)(sol)] (M = Fe(III), Mn(III)) complexes exhibit solvent-dependent cooperative transformations between nonpolar and polar molecular assemblies with distinct metal ion-dependent behaviours. The Fe(III) complexes readily formed polar aggregates upon DMSO coordination, giving rise to strong SHG response, enhanced dielectric constant, and ferroelectric-like relaxor behaviour. By contrast, the Mn(III) complexes adopted centrosymmetric dimers stabilized by Jahn–Teller distortions, leading to nonpolar packing and SHG inactivity. These findings reveal a clear correlation between the properties of the metal centre, ligand architecture, and aggregation-induced functionality, providing fundamental insights for rational design of multifunctional molecular materials.

These results suggest that solvent-vapour-induced transformations may provide a possible approach for integrating optical and polar functionalities, and potentially magnetic properties, within a single coordination framework. Future studies will focus on chiral derivatives, thin-film processing, and mixed-metal systems to optimise ferroelectric switching, SHG activity, and magnetic ordering, paving the way for the development of stimuli-responsive molecular solids with tuneable multifunctional properties.

Experimental

General

All reagents and solvents were obtained from Tokyo Kasei Co. and Wako Pure Chemical Industries and were reagent grade and used without further purification. All reactions were carried out under ambient atmosphere.

Syntheses

H_2azdp (=2,2′-azodiphenol) ligand was purchased commercially.

[Fe(azdp)(acac)(MeOH)] (1). An $Fe(acac)_3$ (1.05 g, 3.0 mmol) and H_2azdp (0.64 g, 3.0 mmol) were dissolved in methanol (30 mL) and refluxed for 1 h. After stirring the solution at room temperature for 1 d, **1** was obtained as a black microcrystal. The samples were collected by suction filtration, washed with a small amount of diethyl ether, and air-dried. Yield: 1.02 g (88%). Suitable crystals for the single-crystal XRD measurements were synthesised by recrystallizing from MeOH, and the solution was allowed to stand for a few days during which black block crystals formed. Anal. calc. for **1** ($C_{18}H_{19}N_2FeO_5$): C, 54.16; H, 4.80; N, 7.02. Found: C, 53.99; H, 4.79; N, 7.11%. IR (KBr/cm^{-1}): 1591, 1570, 1533, 1475, 1448, 1381, 1363, 1327, 1298, 1286, 1250, 1238, 1213, 1176, 1151, 1140, 1119, 1038, 1026, 931, 847, 754, 530.

[Mn(azdp)(acac)(MeOH)] (2). $Mn(acac)_3$ (1.05 g, 3.0 mmol) and H_2azdp (0.64 g, 3.0 mmol) were dissolved in methanol (40 mL) and refluxed for 1 h. After stirring the solution at room temperature for 1 d, **2** was obtained as black microcrystals. The samples were collected by suction filtration, washed with a small amount of diethyl ether, and air-dried. Yield: 1.09 g (95%). Suitable crystals for single-crystal XRD measurements were synthesised by recrystallisation from MeOH, and the solution was allowed to stand for a few days, during which black block crystals formed. Anal. calc. for **2** ($C_{18}H_{19}N_2MnO_5$): C, 54.28; H, 4.81; N, 7.03. Found: C, 54.30; H, 4.92; N, 7.13%. IR (KBr/cm^{-1}): 1600, 1583, 1535, 1523, 1469, 1446, 1385, 1327, 1306, 1282, 1261, 1250, 1236, 1213, 1201, 1149, 1141, 1120, 1033, 1028, 926, 847, 760, 750, 538.

[Fe(azdp)(acac)(DMSO)] (3). **3** was obtained by recrystallising [Fe(azdp)(acac)(MeOH)] from a DMSO/MeOH mixed solvent and allowing the solution to stand for a few days, during which black block crystals were formed. The samples were collected by suction filtration, washed with a small amount of diethyl ether, and air-dried. Anal. calc. for **3** ($C_{19}H_{21}N_2FeO_5S$): C, 51.25; H, 4.75; N, 6.29. Found: C, 51.00; H, 4.74; N, 6.37%. IR (KBr/cm^{-1}): 1597, 1587, 1576, 1539, 1523, 1477, 1468, 1450, 1435, 1392, 1367, 1335, 1323, 1296, 1279, 1257, 1146, 1022, 989, 951, 941, 847, 766, 750, 530.

[Mn(azdp)(acac)(DMSO)] (4). **4** was obtained by recrystallising [Mn(azdp)(acac)(MeOH)] from a DMSO/MeOH mixed solvent and allowing the solution to stand for a few days,

during which black block crystals were formed. The samples were collected by suction filtration, washed with a small amount of diethyl ether, and air-dried. Anal. calc. for **4** ($C_{19}H_{21}N_2MnO_5S$): C, 51.35; H, 4.76; N, 6.30. Found: C, 51.15; H, 4.82; N, 6.41%. IR (KBr/cm^{-1}): 1597, 1589, 1570, 1539, 1510, 1468, 1450, 1408, 1390, 1321, 1302, 1282, 1255, 1238, 1213, 1142, 1124, 1007, 955, 924, 847, 765, 752, 742, 544.

Solvent-vapour exposure experiments

A small amount of the ground crystalline samples chosen from **1** and **2** was added to a small glass vial. The vial was placed in a larger capped glass vial with a small amount of the DMSO (*ca.* 2 mL) as the vapour source. The sealed system was allowed to stand at room temperature for several days (25 °C).

Physical measurements

General procedures. Elemental analyses (C, H, N) were performed using a MICRO CORDER JM10 CHN analyser (J-SCIENCE LAB Co., Ltd.). FT-IR spectroscopy was performed with a HORIBA FT-730 instrument equipped using the KBr pellet method. Thermogravimetric (TG) measurements were performed using a Bruker TG-DTA 2010SA instrument.

Single crystal and powder X-ray diffraction. The single-crystal XRD data for all compounds were recorded using a Bruker D8 QUEST diffractometer employing graphite monochromated Mo Kα radiation generated from a sealed tube (λ = 0.7107 Å). Data integration and reduction were performed using APEX4. Using the Olex2 software, the structure was solved with the SHELXT structure solution program using intrinsic-phasing methods and refined with the SHELXL refinement package using least-squares minimisation. Hydrogen atoms were included in idealized positions and refined using a riding model. For all compounds, PXRD data were collected with a Rigaku MiniFlex II ultra (40 kV/15 mA) X-ray diffractometer using Cu Kα radiation (λ = 1.5406 Å) in the 2θ range of 5–30° with a step width of 3.0°.

Dielectric property measurements. Temperature-dependent dielectric constants in the frequency range of 10 Hz to 1 MHz were measured using a Solartron 1260 impedance/gain-phase analyser with a Solartron 1296 dielectric interface (Solartron Co. Ltd).

Second harmonic generation (SHG) measurements. The fundamental output of a Q-switched Nd^{3+}:YAG laser (Continuum, Surelite I) at 1064 nm with a pulse energy of approximately 0.5 mJ was incident on the crystal sample without beam collimation. An infrared cutoff filter was placed after the sample to suppress the residual fundamental radiation while transmitting the visible-wavelength emission. The second-harmonic signal at 532 nm, propagating collinearly with the incident beam, was spectrally dispersed using a monochromator (Bunko Keiki, M25) and detected by a photomultiplier tube (Hamamatsu Photonics, R928). The detected signal was amplified by a preamplifier (Stanford Research Systems, SR240), accumulated using a boxcar integrator (Stanford Research Systems, SR250), and subsequently recorded on a personal computer.

Author contributions

F. K. and M. T. planned and directed the project, and H. I. synthesised the compounds and carried out all measurements. S. H. conducted the SHG measurements. F. K. drafted the manuscript, and all authors contributed to revising the manuscript.

Conflicts of interest

There are no conflicts to declare.

Data availability

The data supporting this article have been included as part of the Supplementary Information (SI).

Supplementary information: crystallographic data, PXRD patterns, IR spectra, Crystal structures, TGA. See DOI: https://doi.org/10.1039/d5ce01141h.

CCDC 2512678–2512681 (**1**–**4**) contain the supplementary crystallographic data for this paper.[55a–d]

Acknowledgements

This work was supported by the JSPS KAKENHI Grant-in-Aid for Early-Career Scientists JP23K13767 and JP25K18052 from the Ministry of Education, Culture, Sports, Science, and Technology, Japan. This work was also supported by the Iketani Science and Technology Foundation.

Notes and references

1 W. Huang, X. Ma, O. Sato and D. Wu, *Chem. Soc. Rev.*, 2021, **50**, 6832–6870.
2 S. Horiuchi and Y. Tokura, *Nat. Mater.*, 2008, **7**, 357–366.
3 S. Horiuchi, Y. Tokunaga, G. Giovannetti, S. Picozzi, H. Itoh, R. Shimano, R. Kumai and Y. Tokura, *Nature*, 2010, **463**, 789–792.
4 A. S. Tayi, A. Kaeser, M. Matsumoto, T. Aida and S. I. Stupp, *Nat. Chem.*, 2015, **7**, 281–294.
5 R. A. Wiscons, N. R. Goud, J. T. Damron and A. J. Matzger, *Angew. Chem., Int. Ed.*, 2018, **57**, 9044–9047.
6 P. P. Shi, Y. Y. Tang, P. F. Li, W. Q. Liao, Z. X. Wang, Q. Ye and R. G. Xiong, *Chem. Soc. Rev.*, 2016, **45**, 3811–3827.
7 Y. Sekine, R. Akiyoshi and S. Hayami, *Coord. Chem. Rev.*, 2022, **469**, 214663.
8 R. Akiyoshi and S. Hayami, *Chem. Commun.*, 2022, **58**, 8309–8321.
9 H. Kobayashi, A. Kobayashi and H. Tajima, *Chem. – Asian J.*, 2011, **6**, 1688–1704.
10 A. Ueda, *Bull. Chem. Soc. Jpn.*, 2017, **90**, 1181–1188.
11 L. Martin, *Coord. Chem. Rev.*, 2018, **376**, 277–291.
12 M. Wang, Z.-Y. Li, R. Ishikawa and M. Yamashita, *Coord. Chem. Rev.*, 2021, **435**, 213819.
13 C. J. Kousseff, R. Halaksa, Z. S. Parr and C. B. Nielsen, *Chem. Rev.*, 2022, **122**, 4397–4419.
14 O. Sato, J. Tao and Y. Z. Zhang, *Angew. Chem., Int. Ed.*, 2007, **46**, 2152–2187.

15 S. Hayami, K. Hiki, T. Kawahara, Y. Maeda, D. Urakami, K. Inoue, M. Ohama, S. Kawata and O. Sato, *Chem. – Eur. J.*, 2009, **15**, 3497–3508.
16 X. Feng, C. Mathoniere, R. Jeon Ie, M. Rouzieres, A. Ozarowski, M. L. Aubrey, M. I. Gonzalez, R. Clerac and J. R. Long, *J. Am. Chem. Soc.*, 2013, **135**, 15880–15884.
17 E. Milin, V. Patinec, S. Triki, E. E. Bendeif, S. Pillet, M. Marchivie, G. Chastanet and K. Boukheddaden, *Inorg. Chem.*, 2016, **55**, 11652–11661.
18 H. Zheng, Y. S. Meng, G. L. Zhou, C. Y. Duan, O. Sato, S. Hayami, Y. Luo and T. Liu, *Angew. Chem., Int. Ed.*, 2018, **57**, 8468–8472.
19 H. Y. Sun, Y. S. Meng and T. Liu, *Chem. Commun.*, 2019, **55**, 8359–8373.
20 M. Arczynski, J. Stanek, B. Sieklucka, K. R. Dunbar and D. Pinkowicz, *J. Am. Chem. Soc.*, 2019, **141**, 19067–19077.
21 I. C. Berdiell, T. Hochdorffer, C. Desplanches, R. Kulmaczewski, N. Shahid, J. A. Wolny, S. L. Warriner, O. Cespedes, V. Schunemann, G. Chastanet and M. A. Halcrow, *J. Am. Chem. Soc.*, 2019, **141**, 18759–18770.
22 O. S. Wenger, *Chem. Rev.*, 2013, **113**, 3686–3733.
23 M. Yoshida and M. Kato, *Coord. Chem. Rev.*, 2018, **355**, 101–115.
24 A. Kobayashi, S.-i. Imada, Y. Shigeta, Y. Nagao, M. Yoshida and M. Kato, *J. Mater. Chem. C*, 2019, **7**, 14923–14931.
25 E. Li, K. Jie, M. Liu, X. Sheng, W. Zhua and F. Huang, *Chem. Soc. Rev.*, 2020, **49**, 1517–1544.
26 N. Mirzadeh, S. H. Privér, A. J. Blake, H. Schmidbaur and S. K. Bhargava, *Chem. Rev.*, 2020, **120**, 7551–7591.
27 E. Resines-Urien, E. Fernandez-Bartolome, A Martinez-Martinez, A. Gamonal, L. Piñeiro-Lopéz and J. S. Costa, *Chem. Soc. Rev.*, 2023, **52**, 705–727.
28 J. S. Costa, S. Rodriguez-Jimenez, G. A. Craig, B. Barth, C. M. Beavers, S. J. Teat and G. Aromi, *J. Am. Chem. Soc.*, 2014, **136**, 3869–3874.
29 S. Rodriguez-Jimenez, H. L. C. Feltham and S. Brooker, *Angew. Chem., Int. Ed.*, 2016, **55**, 15067–15071.
30 P. Kar, M. Yoshida, Y. Shigeta, A. Usui, A. Kobayashi, T. Minamidate, N. Matsunaga and M. Kato, *Angew. Chem., Int. Ed.*, 2017, **56**, 2345–2349.
31 D. Shao, L. Shi, L. Yin, B. L. Wang, Z. X. Wang, Y. Q. Zhang and X. Y. Wang, *Chem. Sci.*, 2018, **9**, 7986–7991.
32 D. Shao, L. Shi, F. X. Shen, X. Q. Wei, O. Sato and X. Y. Wang, *Inorg. Chem.*, 2019, **58**, 11589–11598.
33 M. Nakaya, R. Ohtani and S. Hayami, *Eur. J. Inorg. Chem.*, 2020, 3709–3719.
34 F. Kobayashi, Y. Komatsumaru, R. Akiyoshi, M. Nakamura, Y. Zhang, L. F. Lindoy and S. Hayami, *Inorg. Chem.*, 2020, **59**, 16843–16852.
35 F. Kobayashi, K. Iwaya, H. Zenno, M. Nakamura, F. Li and S. Hayami, *Bull. Chem. Soc. Jpn.*, 2021, **94**, 158–163.
36 H. Zenno, F. Kobayashi, M. Nakamura, Y. Sekine, L. F. Lindoy and S. Hayami, *Dalton Trans.*, 2021, **50**, 7843–7853.
37 D. Shao, W.-J. Tang, Z. Ruan, X. Yang, L. Shi, X.-Q. Wei, Z. Tian, K. Kumari and S. K. Singh, *Inorg. Chem. Front.*, 2022, **9**, 6147–6157.
38 S. Kusumoto, K. Inaba, H. Suda, M. Nakaya, R. Tokunaga, P. Thuéry, R. Haruki, T. Kanazawa, S. Nozawa, Y. Kim, S. Hayami and Y. Koide, *Inorg. Chem.*, 2023, **62**, 16222–16227.
39 H.-B. Cui, Z. Wang, K. Takahashi, Y. Okano, H. Kobayashi and A. Kobayashi, *J. Am. Chem. Soc.*, 2006, **128**, 15074–15075.
40 H. Zhao, X. Kong, H. Li, Y. Jin, L. Long, X. C. Zeng, R. Huang and L. Zheng, *Proc. Natl. Acad. Sci. U. S. A.*, 2011, **108**, 3481–3486.
41 H. Cui, B. Zhou, L.-S. Long, Y. Okano, H. Kobayashi and A. Kobayashi, *Angew. Chem., Int. Ed.*, 2008, **47**, 3376–3380.
42 X. Y. Dong, B. Li, B. B. Ma, S. J. Li, M. M. Dong, Y. Y. Zhu, S. Q. Zang, Y. Song, H. W. Hou and T. C. Mak, *J. Am. Chem. Soc.*, 2013, **135**, 10214–10217.
43 J. Yanagisawa, K. Tanaka, H. Kano, K. Miyata, B. Le Ouay, R. Ohtani and M. Ohba, *Inorg. Chem.*, 2022, **61**, 15638–15644.
44 J. Yanagisawa, T. Aoyama, K. Fujii, M. Yashima, Y. Inaguma, A. Kuwabara, K. Shitara, B. Le Ouay, S. Hayami, M. Ohba and R. Ohtani, *J. Am. Chem. Soc.*, 2024, **146**, 1476–1483.
45 Y. Shi, Y. Iwai, B. L. Quay, M. Ohba and R. Ohtani, *Eur. J. Inorg. Chem.*, 2025, **28**, e202500059.
46 F. Kobayashi, R. Akiyoshi, D. Kosumi, M. Nakamura, L. F. Lindoy and S. Hayami, *Chem. Commun.*, 2020, **56**, 10509–10512.
47 F. Kobayashi, M. Gemba, S. Hoshino, K. Tsukiyama, M. Shiotsuka, T. Nakajima and M. Tadokoro, *Chem. – Eur. J.*, 2023, **29**, e2022039377.
48 F. Kobayashi, A. Yoshida, M. Gemba, Y. Takatsu and M. Tadokoro, *Dalton Trans.*, 2024, **53**, 11689–11696.
49 M. J. Prakash and T. P. Radhakrishnan, *Chem. Mater.*, 2006, **18**, 2943–2949.
50 L.-L. Chu, T. Zhang, Y.-F. Gao, W.-Y. Zhang, P.-P. Shi, Q. Ye and D.-W. Fu, *Chem. Mater.*, 2020, **32**, 6968–6974.
51 Y. Y. Tang, J. C. Liu, Y. L. Zeng, H. Peng, X. Q. Huang, M. J. Yang and R. G. Xiong, *J. Am. Chem. Soc.*, 2021, **143**, 13816–13823.
52 J. Harada, M. Ohtani, Y. Takahashi and T. Inabe, *J. Am. Chem. Soc.*, 2015, **137**, 4477–4486.
53 S. Furukawa, J. Wu, M. Koyama, K. Hayashi, N. Hoshino, T. Takeda, Y. Suzuki, J. Kawamata, M. Saito and T. Akutagawa, *Nat. Commun.*, 2021, **12**, 21019.
54 Y. Yakiyama, M. Li, D. Zhou, T. Abe, C. Sato, K. Sambe, T. Akutagawa, T. Matsumura, N. Matubayasi and H. Sakurai, *J. Am. Chem. Soc.*, 2024, **146**, 5224–5231.
55 (*a*) CCDC 2512678: Experimental Crystal Structure Determination, 2026, DOI: 10.5517/ccdc.csd.cc2qbn4w; (*b*) CCDC 2512679: Experimental Crystal Structure Determination, 2026, DOI: 10.5517/ccdc.csd.cc2qbn5x; (*c*) CCDC 2512680: Experimental Crystal Structure Determination, 2026, DOI: 10.5517/ccdc.csd.cc2qbn6y; (*d*) CCDC 2512681: Experimental Crystal Structure Determination, 2026, DOI: 10.5517/ccdc.csd.cc2qbn7z.